

Deformation localisation in stretched liquid crystal elastomers

Rabin Poudel* Yasemin Şengül* L. Angela Mihai*

**School of Mathematics, Cardiff University, Cardiff, UK*

June 11, 2024

Abstract

We model within the framework of finite elasticity two inherent instabilities observed in liquid crystal elastomers under uniaxial loads. First is necking which occurs when a material sample suddenly elongates more in a small region where it appears narrower than the rest of the sample. Second is shear striping, which forms when the in-plane director rotates gradually to realign and become parallel with the applied force. These phenomena are due to the liquid crystal molecules rotating freely under mechanical loading. To capture necking, we assume that the uniaxial order parameter increases with tensile stretch, as reported experimentally during polydomain-monodomain transition. To account for shear striping, we maintain the uniaxial order parameter fixed, as suggested by experiments. Our finite element simulations capture well these phenomena. As necking in liquid crystal elastomers has not been satisfactorily modelled before, our theoretical and numerical findings related to this effect can be of wide interest. Shear striping has been well studied, yet our computed examples also show how optimal stripe width increases with the nematic penetration depth measuring the competition between the Frank elasticity of liquid crystals and polymer elasticity. Although known theoretically, this result has not been confirmed numerically by previous nonlinear elastic models.

Key words: nematic elastomers, mathematical models, large-strain deformation, necking, shear striping, finite elements.

1 Introduction

Liquid crystal elastomers (LCEs) are formed from cross-linked polymeric chains with embedded liquid crystal (LC) molecules [47]. Due to this special architecture, they display both self-organisation under external stimuli, such as heating or illumination, and large reversible deformations under mechanical loads. In modern laboratories, LCEs are being prepared through various techniques. Typically, polydomain samples are obtained where the material contains multiple subdomains, with a different nematic alignment. The unit vector for the localised direction of uniaxial nematic alignment is termed the *director*. Monodomain LCEs can subsequently be achieved by applying electric or magnetic fields, or deforming the material mechanically to induce a desired nematic orientation.

There has been a long-standing interest in the multi-physics characteristics of nematic elastomers and incorporating them in muscle-like actuators and other advanced technologies [8, 21, 41, 48]. However, many fundamental questions concerning these material remain open and require further theoretical investigation.

Generally, under mechanical loads, the nematic director tends to rotate in order to align with the largest principal stretch [30, 36]. This rotation is not always uniform and can generate some interesting macroscopic effects. For example, when subject to a large tensile force, some LCEs exhibit localised necking [5, 6]. This phenomenon occurs when there is a critical extension ratio, such that the force required to extend the material beyond this critical value changes from increasing to decreasing. In

this case, the homogeneous deformation becomes unstable, and the material sample suddenly elongates more in a small region than in the rest of the sample. Locally, the material appears much narrower than before the critical stretch was reached, as illustrated schematically in Figure 1. Experimental evidence of LCE necking has been reported in [19, 20, 26]. Also, in [19], since necking could not be captured by the neoclassical LCE model based on the neo-Hookean strain-energy function for rubber, it was suggested that a viscoelastic model would be required instead. A finite element modelling of instabilities in viscoelastic nematic elastomers, including necking, is presented in [4]. However, within the theoretical framework of elasticity, a satisfactory mathematical model for LCE necking is still to be achieved.

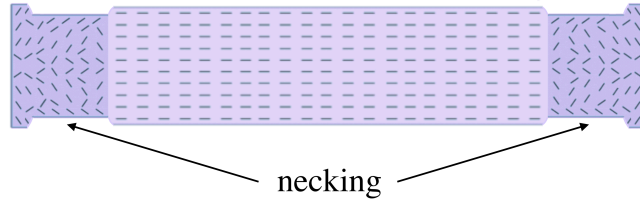


Figure 1: Schematics of nematic LCE developing necking under large stretch causing the initially disordered LC molecules to rotate until they align with the applied force in the horizontal direction. Darker colour at the ends signifies opacity in the physical sample where the LC molecules are randomly oriented, while the lighter colour in the middle corresponds to the physical sample being translucent where the LC molecules are uniformly aligned.

Certain stretch deformations of LCEs also result in a pattern of parallel stripe subdomains where equal and opposite shear deformations occur in neighbouring stripes [18, 22]. The theoretical explanation for this phenomenon, which is depicted schematically in Figure 2, is that the energy depending isotropically on the macroscopic deformation through the relative strain of the microstructure is minimised by a state of many homogeneously deformed parts. This is known as *soft* or *semi-soft elasticity*, since it is usually accompanied by a much slower increase in the required stress compared to prior and subsequent deformed states [3]. Shear stripes formation in elongated nematic LCEs [13, 20, 22, 23, 38, 39, 44, 50] has been extensively analysed theoretically [1–3, 7, 10, 11, 15–17, 22, 30–33, 35] or simulated numerically [29, 43], and it is therefore well understood.

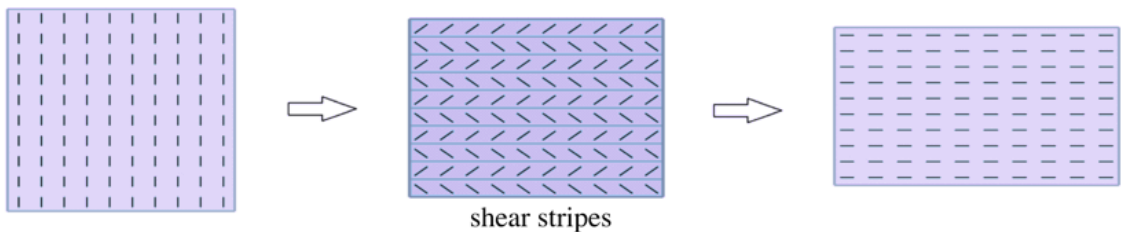


Figure 2: Schematics of nematic LCE developing shear stripes under large stretch causing the initial director in the vertical direction to rotate until it aligns with the applied force in the horizontal direction. Darker colour in the middle figure signifies opacity in the physical sample where the shear stripes form, while lighter colour in the left- and right-hand figures corresponds to the physical sample being translucent where the LC molecules are uniformly aligned.

In this paper, first we introduce a theoretical model for LCEs capable of necking under uniaxial tensile load (Section 2). We then revisit the modelling of LCE shear striping under uniaxial tension, providing an analytical solution and estimating stripe periodicity [46] (Section 3). These models are further implemented in a finite element code to simulate the respective effects (Section 4). Necking in LCEs has not been satisfactorily modelled before, so both our theoretical and numerical findings related to this effect can be of wide interest. While shear striping has been well studied, our numerical

examples also show how optimal stripe width increases with the nematic penetration depth measuring the competition between the Frank elasticity of LCs and polymer elasticity. This result, although known theoretically, has not been captured numerically by previous nonlinear elastic models.

2 Necking

To describe an incompressible nematic LCE, we consider the following strain-energy function [17]

$$W^{(lce)} = \frac{\mu^{(1)}}{2} (\lambda_1^2 + \lambda_2^2 + \lambda_3^2 - 3) + \frac{\mu^{(2)}}{2} (\alpha_1^2 + \alpha_2^2 + \alpha_3^2 - 3), \quad (1)$$

where $\mu = \mu^{(1)} + \mu^{(2)} > 0$ is the shear modulus at infinitesimal strain, with $\mu^{(1)}, \mu^{(2)} \geq 0$ constant material parameters, $\{\lambda_1^2, \lambda_2^2, \lambda_3^2\}$ denote the eigenvalues of $\mathbf{F}\mathbf{F}^T$, with \mathbf{F} the deformation gradient from the reference cross-linking state, satisfying $\det \mathbf{F} = 1$, and $\{\alpha_1^2, \alpha_2^2, \alpha_3^2\}$ represent the eigenvalues of $\mathbf{A}\mathbf{A}^T$, with $\mathbf{A} = \mathbf{G}^{-1}\mathbf{F}\mathbf{G}_0$ the local elastic deformation tensor satisfying $\det \mathbf{A} = 1$, while \mathbf{G}_0 and \mathbf{G} are the natural deformation tensors due to the nematic director in the reference and current configuration, respectively.

Assuming that the LCE is intrinsically uniaxial, the natural deformation tensor takes the form

$$\mathbf{G} = a^{-1/6}\mathbf{I} + \left(a^{1/3} - a^{-1/6}\right)\mathbf{n} \otimes \mathbf{n}, \quad (2)$$

where \mathbf{n} is the local nematic director, \otimes denotes the tensor product of two vectors, $\mathbf{I} = \text{diag}(1, 1, 1)$ is the identity tensor, and

$$a = \frac{1 + 2Q}{1 - Q} \quad (3)$$

represents the natural shape parameter, with Q the scalar uniaxial order parameter ($Q = 1$ corresponds to perfect nematic order and $Q = 0$ to the case where mesogens are randomly oriented) [9]. For the reference configuration, \mathbf{G} is replaced by \mathbf{G}_0 , with \mathbf{n}_0 , a_0 and Q_0 instead of \mathbf{n} , a and Q , respectively.

Note that, when $\mu^{(2)} = 0$, the phenomenological model in equation (1) reduces to the neo-Hookean model for rubber [45], and when $\mu^{(1)} = 0$, it simplifies to the neoclassical model for LCEs [1, 2].

The nematic elastomer modelled by equation (1) is subject to the finite-strain deformation with $\lambda_1 = \lambda > 1$ and $\lambda_2 = \lambda_3 = \lambda^{-1/2}$, while the tensile force is parallel to the nematic director in the current configuration, so that

$$\mathbf{G} = \text{diag} \left(\left(\frac{1 + 2Q}{1 - Q} \right)^{1/3}, \left(\frac{1 - Q}{1 + 2Q} \right)^{1/6}, \left(\frac{1 - Q}{1 + 2Q} \right)^{1/6} \right). \quad (4)$$

Taking $\mathbf{G}_0 = \mathbf{I}$, we have

$$\lambda_1 = \alpha_1 \left(\frac{1 + 2Q}{1 - Q} \right)^{1/3}, \quad \lambda_2 = \alpha_2 \left(\frac{1 - Q}{1 + 2Q} \right)^{1/6}, \quad \lambda_3 = \alpha_3 \left(\frac{1 - Q}{1 + 2Q} \right)^{1/6}, \quad (5)$$

and

$$\alpha_1 = \lambda \left(\frac{1 + 2Q}{1 - Q} \right)^{-1/3} = \alpha, \quad \alpha_2 = \alpha_3 = \lambda^{-1/2} \left(\frac{1 - Q}{1 + 2Q} \right)^{-1/6} = \alpha^{-1/2}. \quad (6)$$

For uniaxial tension, the principal components of the first Piola-Kirchhoff stress tensor are, respectively,

$$P_1 = \frac{\partial W^{(lce)}}{\partial \lambda_1} - p\lambda_1^{-1} = P > 0, \quad (7)$$

$$P_2 = \frac{\partial W^{(lce)}}{\partial \lambda_2} - p\lambda_2^{-1} = 0, \quad (8)$$

$$P_3 = \frac{\partial W^{(lce)}}{\partial \lambda_3} - p\lambda_3^{-1} = 0, \quad (9)$$

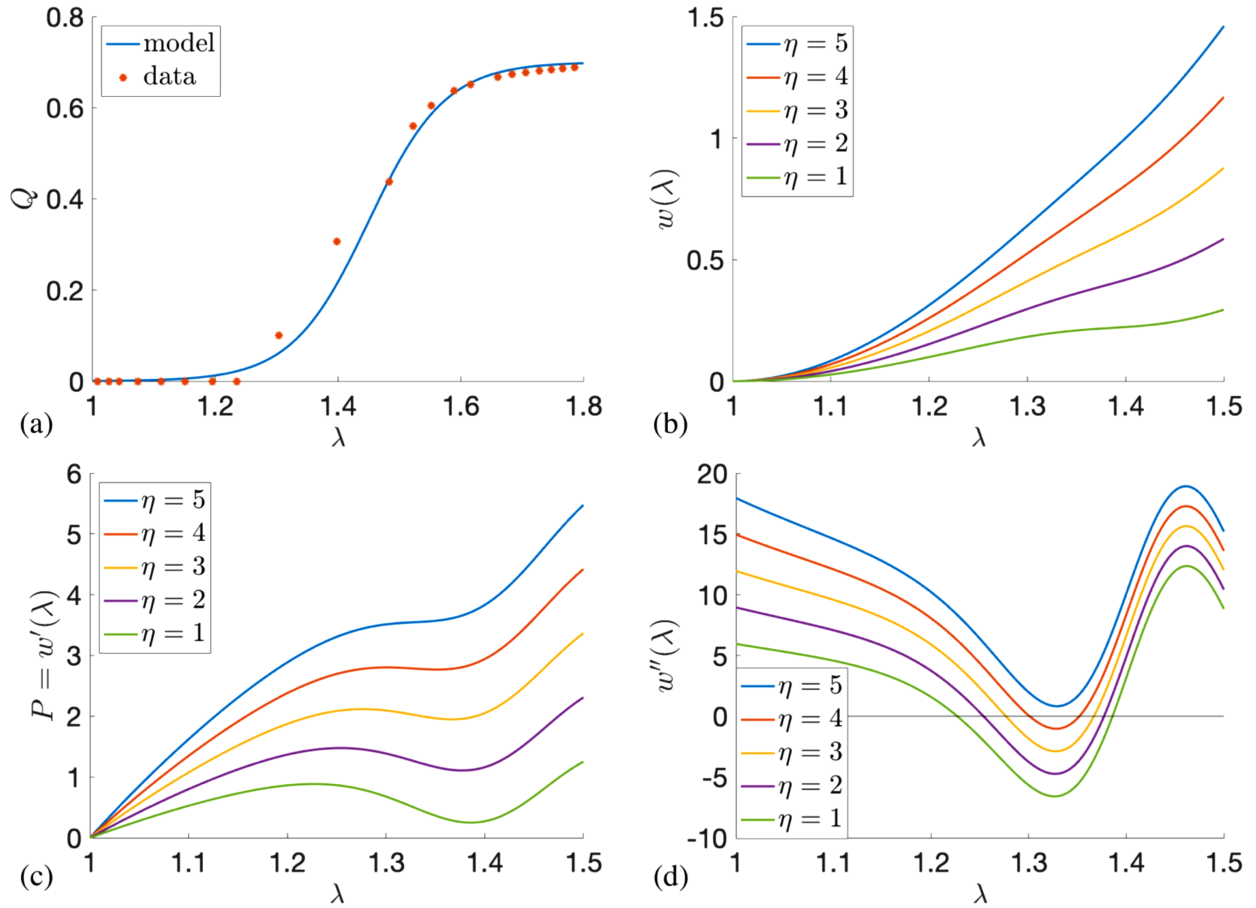


Figure 3: (a) The uniaxial order parameter Q given by equation (11) and the associated experimental data [14]; (b) The nondimensionalised strain-energy function $w(\lambda)$, for different values of $\eta = \mu^{(1)}/\mu^{(2)}$; (c) The applied tensile stress $P = w'(\lambda)$; (d) The second derivative $w''(\lambda)$ of the strain-energy function $w(\lambda)$.

where p is the Lagrange multiplier for the incompressibility constraint, also known as the *arbitrary hydrostatic pressure* [30].

We denote by $w(\lambda)$ the strain-energy function given by equation (1) with λ as the only variable. Then the first derivative of this function is equal to the applied tensile stress, i.e.,

$$w'(\lambda) = (P_1 + p\lambda_1^{-1}) \frac{\partial \lambda_1}{\partial \lambda} + p\lambda_2^{-1} \frac{\partial \lambda_2}{\partial \lambda} + p\lambda_3^{-1} \frac{\partial \lambda_3}{\partial \lambda} = P, \quad (10)$$

and necking forms when the applied stress P first increases, then decreases, then increases again as λ increases [30]. It can be shown that, when Q is constant, $w''(\lambda) > 0$, therefore necking cannot occur if Q is independent of deformation. A more general result is proved in Appendix A of this paper.

We let Q depend on the deformation through the following relation obtained by calibration to experimental data of [14], as shown in Figure 3(a) (see also Appendix B of this paper):

$$Q = 0.35 \left[\frac{e^{16(\lambda-1.45)} - 1}{e^{16(\lambda-1.45)} + 1} - \frac{e^{16} - 1}{e^{16} + 1} + 2 \right], \quad \text{for } \lambda \geq 1. \quad (11)$$

It remains to verify numerically that the second derivative $w''(\lambda)$ of $w(\lambda)$ will change sign for some $\lambda \in (1, 2)$. For different values of η , the nondimensionalised function $w(\lambda)$ (i.e., the function divided by $\mu^{(2)}$) and its first two derivatives are plotted in Figure 3(b)-(d), respectively. These plots suggest that, as η increases, the necking interval (i.e., the interval where $w''(\lambda) < 0$) decreases, and there is a critical value $\eta_{crt} \approx 4.55$ above which necking does not form. For example, when $\eta = \mu^{(1)}/\mu^{(2)} = 3$, $w''(\lambda)$ changes from positive to negative at $\lambda_* \approx 1.28$, then from negative to positive at $\lambda^* \approx 1.37$. In this case, necking occurs for $1.28 < \lambda < 1.37$. When $\eta \rightarrow \infty$, the model reduces to the neo-Hookean model for rubber, which does not exhibit necking.

3 Shear striping

Next, we analyse shear striping under uniaxial stress, where $\lambda_1 = \lambda$ and $\lambda_2 = \lambda_3 = \lambda^{-1/2}$. In this case, we assume that the nematic director only rotates in the biaxial plane while the uniaxial order parameter Q remains constant. This assumption about the order parameter is consistent with experimental observations showing relatively small variations before, during and after stripe formation [20, 22, 44, 50].

In a Cartesian system of coordinates, we define the nematic director in the reference and stretched configuration, respectively, as

$$\mathbf{n}_0 = \begin{bmatrix} 1 \\ 0 \\ 0 \end{bmatrix}, \quad \mathbf{n} = \begin{bmatrix} \cos \theta \\ \sin \theta \\ 0 \end{bmatrix}, \quad (12)$$

where $\theta \in [0, \pi/2]$ is the angle between \mathbf{n} and \mathbf{n}_0 . The associated natural deformation tensors take the form, respectively,

$$\mathbf{G}_0 = \begin{bmatrix} a^{1/3} & 0 & 0 \\ 0 & a^{-1/6} & 0 \\ 0 & 0 & a^{-1/6} \end{bmatrix} \quad (13)$$

and

$$\mathbf{G} = \begin{bmatrix} a^{-1/6} + (a^{1/3} - a^{-1/6}) \cos^2 \theta & (a^{1/3} - a^{-1/6}) \sin \theta \cos \theta & 0 \\ (a^{1/3} - a^{-1/6}) \sin \theta \cos \theta & a^{-1/6} + (a^{1/3} - a^{-1/6}) \sin^2 \theta & 0 \\ 0 & 0 & a^{-1/6} \end{bmatrix}. \quad (14)$$

To demonstrate shear striping, following the procedure in [31–33], we consider the following perturbed deformation gradient

$$\mathbf{F} = \begin{bmatrix} \lambda^{-1/2} & 0 & 0 \\ \varepsilon & \lambda & 0 \\ 0 & 0 & \lambda^{-1/2} \end{bmatrix}, \quad (15)$$

where $\lambda > 1$ is the stretch ratio in the applied tensile force direction, and $0 < \varepsilon \ll 1$ is a small shear parameter. The elastic deformation tensor is then equal to

$$\mathbf{A} = \begin{bmatrix} \lambda^{-1/2} (a^{1/2} \sin^2 \theta + \cos^2 \theta) & \lambda (a^{-1/2} - 1) \sin \theta \cos \theta & 0 \\ \lambda^{-1/2} (1 - a^{1/2}) \sin \theta \cos \theta & \lambda (a^{-1/2} \sin^2 \theta + \cos^2 \theta) & 0 \\ 0 & 0 & \lambda^{-1/2} \end{bmatrix} + \varepsilon \begin{bmatrix} (1 - a^{1/2}) \sin \theta \cos \theta & 0 & 0 \\ (\sin^2 \theta + a^{1/2} \cos^2 \theta) & 0 & 0 \\ 0 & 0 & 0 \end{bmatrix}. \quad (16)$$

We denote by $w(\lambda, \varepsilon, \theta)$ the strain-energy function described by equation (1), depending only on λ , ε and θ . This function takes the following form,

$$\begin{aligned} w(\lambda, \varepsilon, \theta) &= \frac{\mu^{(1)}}{2} (\lambda^2 + 2\lambda^{-1} + \varepsilon^2 - 3) \\ &+ \frac{\mu^{(2)}}{2} \left\{ \left[\lambda^{-1/2} (a^{1/2} \sin^2 \theta + \cos^2 \theta) + \varepsilon (1 - a^{1/2}) \sin \theta \cos \theta \right]^2 \right. \\ &+ \left[\lambda^{-1/2} (1 - a^{1/2}) \sin \theta \cos \theta + \varepsilon (\sin^2 \theta + a^{1/2} \cos^2 \theta) \right]^2 \\ &\left. + \left[\lambda (a^{-1/2} - 1) \sin \theta \cos \theta \right]^2 + \left[\lambda (a^{-1/2} \sin^2 \theta + \cos^2 \theta) \right]^2 + \lambda^{-1} - 3 \right\}. \end{aligned} \quad (17)$$

Differentiating with respect to ε and θ , respectively, gives

$$\begin{aligned} \frac{\partial w(\lambda, \varepsilon, \theta)}{\partial \varepsilon} &= \mu^{(1)} \varepsilon \\ &+ \mu^{(2)} \left\{ \left[\lambda^{-1/2} (a^{1/2} \sin^2 \theta + \cos^2 \theta) + \varepsilon (1 - a^{1/2}) \sin \theta \cos \theta \right] (1 - a^{1/2}) \sin \theta \cos \theta \right. \\ &\left. + \left[\lambda^{-1/2} (1 - a^{1/2}) \sin \theta \cos \theta + \varepsilon (\sin^2 \theta + a^{1/2} \cos^2 \theta) \right] (\sin^2 \theta + a^{1/2} \cos^2 \theta) \right\} \end{aligned} \quad (18)$$

and

$$\begin{aligned} \frac{\partial w(\lambda, \varepsilon, \theta)}{\partial \theta} &= \mu^{(2)} \left\{ (a^{1/2} - 1) \left[2\lambda^{-1/2} \sin \theta \cos \theta + \varepsilon (\sin^2 \theta - \cos^2 \theta) \right] \right. \\ &\cdot \left[\lambda^{-1/2} (a^{1/2} \sin^2 \theta + \cos^2 \theta) + \varepsilon (1 - a^{1/2}) \sin \theta \cos \theta \right] \\ &+ (a^{1/2} - 1) \left[\lambda^{-1/2} (\sin^2 \theta - \cos^2 \theta) - 2\varepsilon \sin \theta \cos \theta \right] \\ &\cdot \left[\lambda^{-1/2} (1 - a^{1/2}) \sin \theta \cos \theta + \varepsilon (\sin^2 \theta + a^{1/2} \cos^2 \theta) \right] \\ &\left. + \lambda^2 (a^{-1} - 1) \sin \theta \cos \theta \right\}. \end{aligned} \quad (19)$$

The equilibrium solution satisfies the simultaneous equations for energy minimisation,

$$\frac{\partial w(\lambda, \varepsilon, \theta)}{\partial \varepsilon} = 0 \quad \text{and} \quad \frac{\partial w(\lambda, \varepsilon, \theta)}{\partial \theta} = 0. \quad (20)$$

At $\varepsilon = 0$ and $\theta = 0$, the partial derivatives defined by equations (18)-(19) are equal to zero, i.e., this solution is always an equilibrium state. For sufficiently small values of ε and θ , we can write the second order approximation

$$w(\lambda, \varepsilon, \theta) \approx w(\lambda, 0, 0) + \frac{1}{2} \left(\varepsilon^2 \frac{\partial^2 w}{\partial \varepsilon^2}(\lambda, 0, 0) + 2\varepsilon\theta \frac{\partial^2 w}{\partial \varepsilon \partial \theta}(\lambda, 0, 0) + \theta^2 \frac{\partial^2 w}{\partial \theta^2}(\lambda, 0, 0) \right), \quad (21)$$

where

$$\frac{\partial^2 w}{\partial \varepsilon^2}(\lambda, 0, 0) = \mu^{(1)} + \mu^{(2)} a, \quad (22)$$

$$\frac{\partial^2 w}{\partial \varepsilon \partial \theta}(\lambda, 0, 0) = \mu^{(2)} \lambda^{-1/2} (1 - a), \quad (23)$$

$$\frac{\partial^2 w}{\partial \theta^2}(\lambda, 0, 0) = \mu^{(2)} (\lambda^2 - \lambda^{-1} a) (a^{-1} - 1). \quad (24)$$

First, we find the equilibrium value θ_0 for θ as a function of ε by solving the second equation in (20). By the approximation (21), the corresponding equation takes the form

$$\varepsilon \frac{\partial^2 w}{\partial \varepsilon \partial \theta}(\lambda, 0, 0) + \theta \frac{\partial^2 w}{\partial \theta^2}(\lambda, 0, 0) = 0, \quad (25)$$

implying

$$\theta_0(\varepsilon) = -\varepsilon \frac{\partial^2 w}{\partial \varepsilon \partial \theta}(\lambda, 0, 0) / \frac{\partial^2 w}{\partial \theta^2}(\lambda, 0, 0). \quad (26)$$

Next, substituting $\theta = \theta_0(\varepsilon)$ in (21) yields the following function in ε ,

$$w(\lambda, \varepsilon, \theta_0(\varepsilon)) - w(\lambda, 0, 0) \approx \frac{\varepsilon^2}{2} \left[\frac{\partial^2 w}{\partial \varepsilon^2}(\lambda, 0, 0) - \left(\frac{\partial^2 w}{\partial \varepsilon \partial \theta}(\lambda, 0, 0) \right)^2 / \frac{\partial^2 w}{\partial \theta^2}(\lambda, 0, 0) \right]. \quad (27)$$

Depending on whether the expression on the right-hand side is negative, zero, or positive, the respective equilibrium state is unstable, neutrally stable, or stable. We deduce that the equilibrium state with $\varepsilon = 0$ and $\theta = 0$ is unstable if

$$a^{1/3} \left(\frac{\eta + 1}{\eta + a} \right)^{1/3} < \lambda < a^{1/3}, \quad (28)$$

where $\eta = \mu^{(1)}/\mu^{(2)}$.

Similarly, at $\varepsilon = 0$ and $\theta = \pi/2$, both the partial derivatives defined by (18)-(19) are equal to zero, and

$$\frac{\partial^2 w}{\partial \varepsilon^2}(\lambda, 0, \pi/2) = \mu^{(1)} + \mu^{(2)}, \quad (29)$$

$$\frac{\partial^2 w}{\partial \varepsilon \partial \theta}(\lambda, 0, \pi/2) = \mu^{(2)} \lambda^{-1/2} (a - 1), \quad (30)$$

$$\frac{\partial^2 w}{\partial \theta^2}(\lambda, 0, \pi/2) = \mu^{(2)} (\lambda^2 - \lambda^{-1} a) (1 - a^{-1}). \quad (31)$$

Thus the equilibrium state with $\varepsilon = 0$ and $\theta = \pi/2$ is unstable if

$$a^{1/3} < \lambda < a^{1/3} \left(\frac{\eta + a}{\eta + 1} \right)^{1/3}. \quad (32)$$

Therefore, shear stripes can form when λ satisfies (see also partial results in the Appendix of [31])

$$a^{1/3} \left(\frac{\eta + 1}{\eta + a} \right)^{1/3} < \lambda < a^{1/3} \left(\frac{\eta + a}{\eta + 1} \right)^{1/3}. \quad (33)$$

For the corresponding equilibrium solution, the shear parameter and director angle take the following form, respectively:

$$\varepsilon_0 = \pm \frac{\sqrt{[\lambda^3 (\eta + a) - a (\eta + 1)] [a (\eta + a) - \lambda^3 (\eta + 1)]}}{a \lambda^{1/2} (2\eta + a + 1)}, \quad (34)$$

$$\theta_0 = \pm \arctan \sqrt{\frac{\lambda^3 (\eta + a) - a (\eta + 1)}{a (\eta + a) - \lambda^3 (\eta + 1)}}. \quad (35)$$

The gradient tensors for alternating shear deformations in two adjacent stripe subdomains are \mathbf{F}_\pm with $\varepsilon = \pm \varepsilon_0$, respectively. These two deformations are geometrically compatible in the sense that \mathbf{F}_+ and \mathbf{F}_- are rank-one connected, i.e., $\text{rank}(\mathbf{F}_+ - \mathbf{F}_-) = 1$ [34].

The nondimensionalised strain-energy function $w(\lambda, \varepsilon, \theta)$ (i.e., the function divided by $\mu^{(2)}$) described by equation (17), with $\eta = \mu^{(1)}/\mu^{(2)} = 1$, is illustrated in Figure 4. For λ with values between the lower and upper bounds given by (33), the minimum energy is attained for $(\varepsilon, \theta) = (\varepsilon_0, \theta_0)$ provided by equations (34)-(35). Figure 5 depicts the positive values of the shear parameter ε_0 and director angle θ_0 described by equations (34) and (35), respectively, for different parameter ratios η . When $\eta = 0$, corresponding to the neoclassical form, shear stripes form for $\lambda \in (1, a^{2/3})$. When $\eta \rightarrow \infty$, there is no shear striping since the material is practically purely elastic.

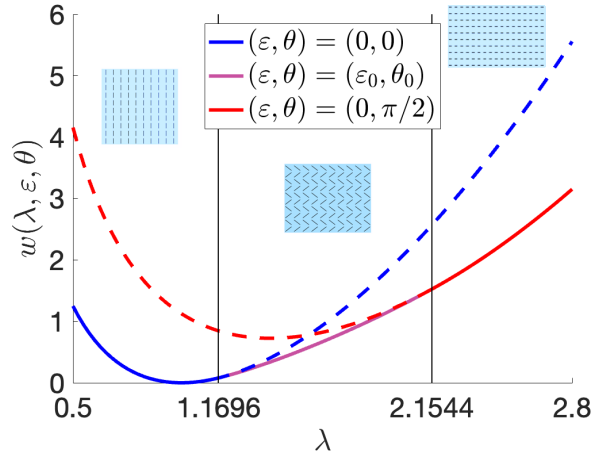


Figure 4: The nondimensionalised strain-energy function $w(\lambda, \varepsilon, \theta)$ given by equation (17), for $(\varepsilon, \theta) = (0, 0)$, $(\varepsilon, \theta) = (\varepsilon_0, \theta_0)$, and $(\varepsilon, \theta) = (0, \pi/2)$, when $a = 4$ and $\eta = 1$ (i.e., $\mu^{(1)} = \mu^{(2)}$). The two vertical lines correspond to the lower and upper bounds on λ . Between these bounds, the second solution, with $(\varepsilon, \theta) = (\varepsilon_0, \theta_0)$, minimises the energy.

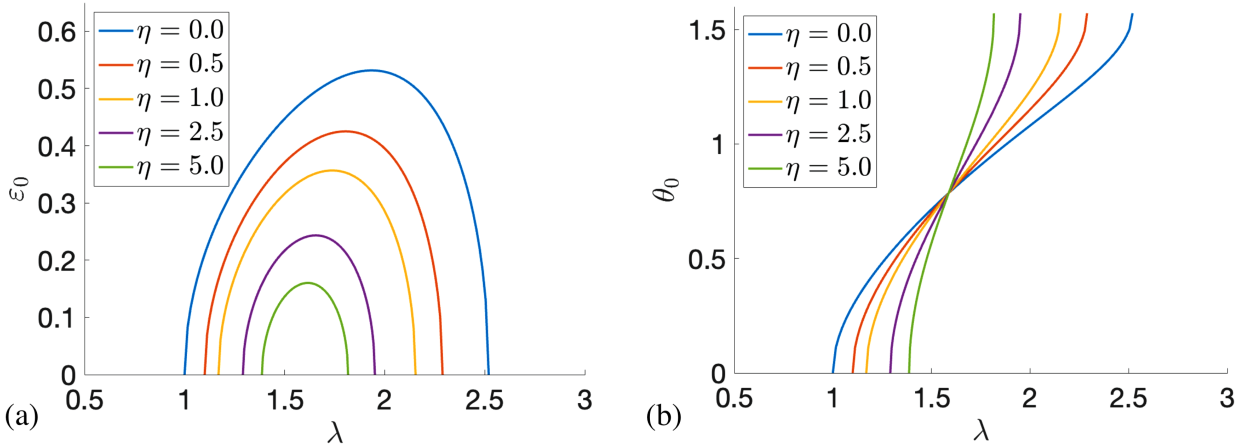


Figure 5: The positive values of the (a) shear parameter ε_0 and (b) director angle θ_0 given by equations (34)-(35), for different values of the parameter ratio $\eta = \mu^{(1)}/\mu^{(2)}$ when $a = 4$.

3.1 Optimal stripe width

For shear striping, the width of each subdomain depends on the material properties, sample geometry and boundary conditions. Dirichlet conditions fixing the director at both ends of the LCE sample in its initial orientation, i.e., perpendicular to the longitudinal direction, known as *strong anchoring*, play an important role in numerically capturing this property. To estimate the stripe width, we add the Frank energy density to our model function, as follows,

$$W^{(nlce)} = W^{(lce)} + \frac{\mathbf{k}}{2} |\mathbf{F}^T \text{Grad } \mathbf{n}|^2, \quad (36)$$

where $W^{(lce)}$ is as defined in equation (1) and \mathbf{k} is the Frank constant [9, 47].

We denote by L_1, L_2, L_3 the size of the undeformed LCE sample in the extension direction (which is perpendicular to the director orientation in the undeformed state), the width direction (which is parallel to the initial director), and the thickness direction, respectively. Provided that Dirichlet boundary conditions are imposed at the ends, the width h of a strip band forming parallel to the initial director at each of these ends must be of the same order of magnitude as that of a shear stripe [46] (see also [47, Appendix C]). For geometric compatibility, the displacement in such a strip band must be equal to γh , where $\gamma = \lambda_{12}(x_1, x_2)$ denotes the shear strain in a shear stripe, so that

$$\frac{d\lambda_{12}}{dx_2} = \frac{d\lambda_{22}}{dx_1}, \quad (37)$$

with $\lambda_{22} \approx h$ representing the stretch ratio in the direction of the stripe width.

Due to the infinitesimal scale of the strip band width, the linear elastic framework is suitable to analyse their deformation. The corresponding elastic energy is then approximately

$$E_{end} \approx \frac{1}{2} \mu \gamma^2 (2L_3 h^2) \frac{L_2}{h} = \mu \gamma^2 L_2 L_3 h, \quad (38)$$

where $L_3 h^2$ is the volume of one end region for a single shear stripe and L_2/h is the number of stripes. This elastic energy decreases as h decreases.

There is additional elastic energy at the narrow interface between adjacent stripes with opposite shear deformation and director rotation. Since the director angle $\theta \in (-\theta_0, \theta_0)$ varies from one side of the interface to the other, so that it takes the value zero in the middle of the interval, this energy is approximately

$$E_{int} \approx L_1 L_3 \sqrt{\mu \mathbf{k}} \left(\frac{L_2}{h} - 1 \right), \quad (39)$$

where $\sqrt{\mu \mathbf{k}}$ is the effective surface tension, $L_1 L_3$ is the area of a single interface, and $L_2/h - 1$ is the number of interfaces. This energy tends to decrease when h increases.

The problem is then to find the optimal stripe width h that minimises the total energy

$$E_{stripe} = E_{end} + E_{int}. \quad (40)$$

Differentiating the above function with respect to h and solving for the critical value, we obtain

$$h \approx \left(L \sqrt{\frac{\mathbf{k}}{\mu}} \right)^{1/2}, \quad (41)$$

i.e., the stripe width increases with sample initial length $L_1 = L$ and nematic penetration depth $\sqrt{\mathbf{k}/\mu} \approx 10^{-8}$ m, which measures the competition between polymer and Frank elasticity. A typical value for the stripe width is $h \approx 10^{-5}$ m.

4 Numerical simulations

We illustrate numerically first the stretch deformation causing necking, then the periodic shear striping for nematic LCEs.

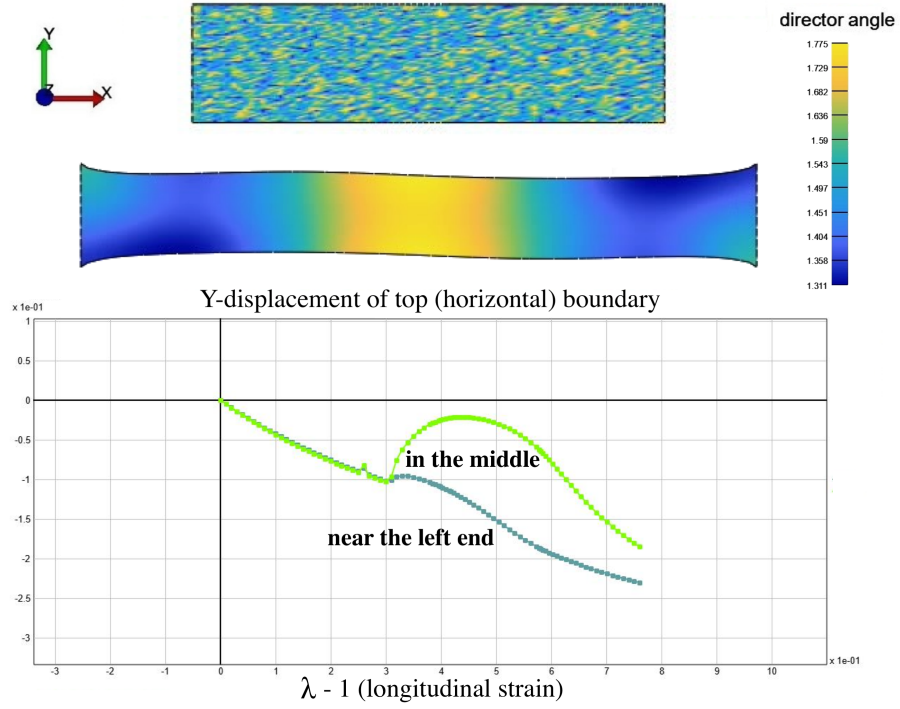


Figure 6: Finite element simulation of necking in a nematic LCE described by equation (1) when $\eta = \mu^{(1)}/\mu^{(2)} = 3$. Top image shows the reference configuration, middle image shows the deformed state with the director orientation, and bottom plot is for the vertical displacement in the middle and near the left end of the top horizontal boundary.

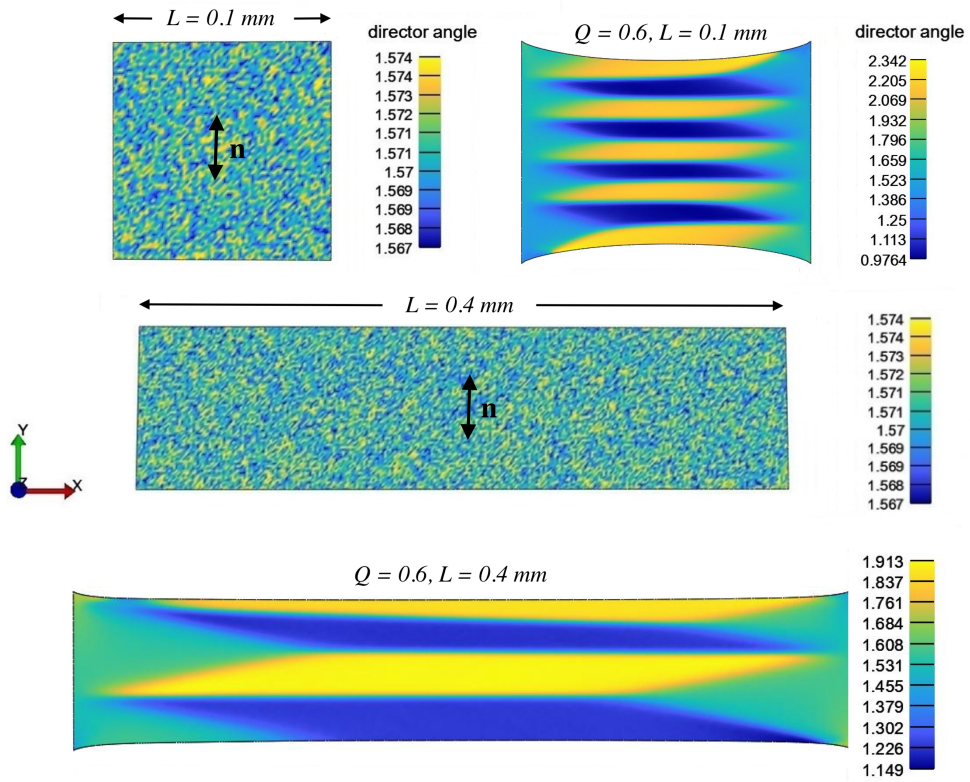


Figure 7: Finite element simulation of nematic LCEs described by equation (36), with $\eta = \mu^{(1)}/\mu^{(2)} = 1$, where stripe width increases with the sample initial length L . Both the reference and deformed configurations are shown.

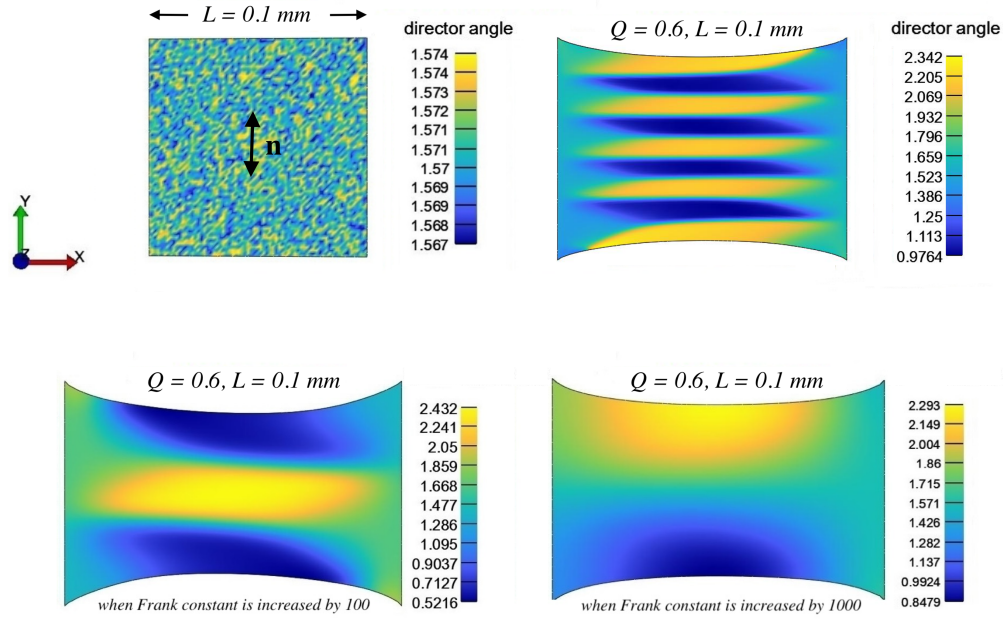


Figure 8: Finite element simulation of nematic LCEs described by equation (36), with $\eta = \mu^{(1)}/\mu^{(2)} = 1$, where stripe width increases with the nematic penetration depth $\sqrt{k/\mu}$ ($\mu = \mu^{(1)} + \mu^{(2)}$). Both the reference and deformed configurations are shown.

Figure 6 presents a finite element simulation of necking where the model function is given by equation (1) with $3\mu^{(1)} = \mu^{(2)} = 10^4$ Pa. In this figure, the deformed configuration appears narrower near the ends than in the middle. This is confirmed by the plots showing the corresponding vertical displacements as stretching increases. The darker colour at the ends of the deformed state further suggest that the director is less aligned with the tensile direction compared to the middle section.

Figures 7-8 show finite element examples of shear striping in a nematic LCE described by equation (36) with $\mu^{(1)} = \mu^{(2)} = 5 \cdot 10^4$ Pa and $k = 10^{-11}$ N. In Figure 7, for two samples with different aspect ratios, the number of stripes reduces almost by half when the initial length L increases 4 times. In Figure 8, the number of stripes reduces by ≈ 3 when Frank constant k increases 100 times, and by ≈ 5 when Frank constant increases 1,000 times. This is in agreement with the estimate of equation (41).

The computed examples presented here were realised by building on existing procedures for three-dimensional finite elasticity of the open-source software Finite Elements for Biomechanics (FEBio) [28]. In addition, our numerical implementation accounts also for macroscopic nematic effects in continuum LCE models [27]. Under uniaxial stretch [47], Dirichlet boundary conditions are imposed on each side parallel to the Y -directions, where the displacement in all directions is prescribed and the nematic director is fixed, while all the other boundaries are free.

5 Conclusion

We have demonstrate both theoretically and numerically deformation localisation through necking and shear striping in nematic elastomer models under uniaxial tensile stress. For necking, the scalar uniaxial order parameter varies, reflecting the polydomain-monodomain transition under mechanical stretch. For shear striping, the order parameter is fixed. Our finite element simulations capture well both of these phenomena. The modelling approaches adopted here can further be extended to include probabilistic model parameters [30] and strain rate effects [4, 49].

A Nematic elastomer models where necking cannot form

In this appendix, we consider the following strain-energy functions describing a nematic LCE,

$$W^{(nc)}(\mathbf{F}, \mathbf{n}) = W(\mathbf{A}), \quad (\text{A.1})$$

where \mathbf{F} represents the macroscopic deformation gradient from the cross-linking state, \mathbf{n} is the nematic director in the present configuration, and $W(\mathbf{A})$ is the strain-energy density of the isotropic polymer network, depending only on the (local) elastic deformation tensor $\mathbf{A} = \mathbf{G}^{-1}\mathbf{F}\mathbf{G}_0$, with \mathbf{G}_0 and \mathbf{G} the natural deformation tensors due to the liquid crystal director in the reference and current configuration, respectively.

The LCE is subject to the finite-strain deformation with $\lambda_1 = \lambda > 1$ and $\lambda_2 = \lambda_3 = \lambda^{-1/2}$, while the tensile force is parallel to the nematic director. Let $\mathbf{G}_0 = \mathbf{I}$, so that

$$\alpha_1 = \lambda \left(\frac{1+2Q}{1-Q} \right)^{-1/3} = \alpha, \quad \alpha_2 = \alpha_3 = \lambda^{-1/2} \left(\frac{1-Q}{1+2Q} \right)^{-1/6} = \alpha^{-1/2}, \quad (\text{A.2})$$

where $Q \in (0, 1)$ is the scalar uniaxial order parameter in the current configuration.

For hyperelastic materials where the force-extension curve does not have a maximum, the homogeneous deformation is the only absolute minimiser of the elastic energy, hence necking cannot occur [42]. Here, we show that, if Q is constant and the hyperelastic model described by $W(\mathbf{A})$ does not exhibit necking, then the LCE model $W^{(nc)}(\mathbf{F})$ does not present necking either.

To prove this, we denote by $w(\lambda)$ the strain-energy function $W^{(nc)}(\mathbf{F})$ given by equation (A.1), depending only on λ , and by $\tilde{w}(\alpha)$ the strain-energy function $W(\mathbf{A})$ for the underlying polymeric network, depending only on α . Calculating the first and second derivatives, we obtain

$$\frac{dw(\lambda)}{d\lambda} = \frac{d\tilde{w}(\alpha)}{d\alpha} \frac{d\alpha}{d\lambda} = \frac{d\tilde{w}(\alpha)}{d\alpha} \left(\frac{1+2Q}{1-Q} \right)^{-1/3} \quad (\text{A.3})$$

and

$$\frac{d^2w(\lambda)}{d\lambda^2} = \frac{d^2\tilde{w}(\alpha)}{d\alpha^2} \frac{d\alpha}{d\lambda} \left(\frac{1+2Q}{1-Q} \right)^{-1/3} = \frac{d^2\tilde{w}(\alpha)}{d\alpha^2} \left(\frac{1+2Q}{1-Q} \right)^{-2/3} > 0. \quad (\text{A.4})$$

The last inequality holds since, by assumption, there is no necking for the polymeric network, hence $d^2\tilde{w}/d\alpha^2 > 0$. It follows that $d^2w/d\lambda^2 > 0$, i.e., for the LCE described by equation (A.1), necking will not form.

In particular, since incompressible neo-Hookean [45] and Mooney-Rivlin [37, 40] hyperelastic models do not exhibit necking, this property is inherited by the associated LCE models of the form given by equation (A.1) (see also [33] for alternative modelling).

B Experimental data

We present in this appendix the experimental data for scalar uniaxial order parameter used to calibrate the function given in equation (11). These data are plotted in Figure 3(a).

Table B.1: Experimental data [14].

λ longitudinal stretch	Q uniaxial order parameter
1.7853	0.6881
1.7658	0.6860
1.7476	0.6838
1.7281	0.6808
1.7061	0.6772
1.6840	0.6727
1.6606	0.6669
1.6164	0.6514
1.5891	0.6365
1.5526	0.6050
1.5227	0.5595
1.4836	0.4378
1.3989	0.3059
1.3037	0.1000
1.2359	0
1.1955	0
1.1512	0
1.1121	0
1.0743	0
1.0443	0
1.0274	0
1.0091	0

References

- [1] Bladon P, Terentjev EM, Warner M. 1993. Transitions and instabilities in liquid crystal elastomers, *Physical Review E: Rapid Communications* 47(6), 3838-3840 (doi: 10.1103/PhysRevE.47.R3838).
- [2] Bladon P, Terentjev EM, Warner M. 1994. Deformation-induced orientational transitions in liquid crystal elastomers, *Journal de Physique II* 4, 75-91 (doi: 10.1051/jp2:1994100).
- [3] Carlson DE, Fried E, Sellers S. 2002. Force-free states, relative strain, and soft elasticity in nematic elastomers, *Journal of Elasticity* 69, 161-180 (doi: 10.1023/A:1027377904576).
- [4] Chehade AEH, Shen B, Yakacki AM, Nguyen TD, Govindjee S. 2024. Finite element modeling of viscoelastic liquid crystal elastomers, *International Journal for Numerical Methods in Engineering* (doi: 0.1002/nme.7510).
- [5] Clarke SM, Terentjev EM. 1998. Slow stress relaxation in randomly disordered nematic elastomers and gels, *Physical Review Letters* 81(20), 4436-4439 (doi: 10.1103/PhysRevLett.81.4436).
- [6] Clarke SM, Terentjev EM, Kundler I, Finkelmann H. 1998. Texture evolution during the polydomain-monodomain transition in nematic elastomers, *Macromolecules* 31(15), 4862-4872 (doi: 10.1021/ma980195j).
- [7] Conti S, DeSimone A, Dolzmann G. 2002. Soft elastic response of stretched sheets of nematic elastomers: a numerical study, *Journal of the Mechanics and Physics of Solids* 50, 1431-1451 (doi: 10.1016/S0022-5096(01)00120-X).
- [8] de Gennes PG, Hébert M, Kant R. 1997. Artificial muscles based on nematic gels, *Macromolecular Symposia* 113, 39-49 (doi: 10.1002/masy.19971130107).
- [9] de Gennes PG, Prost J. 1993. *The Physics of Liquid Crystals*, 2nd ed, Clarendon Press, Oxford.
- [10] DeSimone A, Dolzmann G. 2000. Material instabilities in nematic elastomers, *Physica D. Non-linear Phenomena* 136(1-2), 175-191 (doi: S0167-2789(99)00153-0).
- [11] DeSimone A, Teresi L. 2009. Elastic energies for nematic elastomers, *The European Physical Journal E* 29, 191-204 (doi: 10.1140/epje/i2009-10467-9).
- [12] Ebralidze TD. 1995. Weigert hologram, *Applied Optics* 34(8), 1357-1362 (doi: 10.1364/AO.34.001357).
- [13] Finkelmann H, Kundler I, Terentjev EM, Warner M. 1997. Critical stripe-domain instability of nematic elastomers, *Journal de Physique II* 7, 1059-1069 (doi: 10.1051/jp2:1997171).
- [14] Fridrikh SV, Terentjev EM. 1999. Polydomain-monodomain transition in nematic elastomers, *Physical Review E* 60, 1847-1857 (doi: 10.1103/PhysRevE.60.1847).
- [15] Fried E, Sellers S. 2004. Free-energy density functions for nematic elastomers, *Journal of the Mechanics and Physics of Solids* 52(7), 1671-1689 (doi: 10.1016/j.jmps.2003.12.005).
- [16] Fried E, Sellers S. 2005. Orientational order and finite strain in nematic elastomers, *The Journal of Chemical Physics* 123(4), 043521 (doi: 10.1063/1.1979479).
- [17] Fried E, Sellers S. 2006. Soft elasticity is not necessary for striping in nematic elastomers, *Journal of Applied Physics* 100, 043521 (doi: 10.1063/1.2234824).
- [18] Golubović L, Lubensky TC. 1989. Nonlinear elasticity of amorphous solids, *Physical Review Letters* 63, 1082-1085 (doi: 10.1103/PhysRevLett.63.1082).
- [19] He X, Zheng Y, He Q, Cai S. 2020. Uniaxial tension of a nematic elastomer with inclined mesogens, *Extreme Mechanics Letters* 40, 100936 (doi: 10.1016/j.eml.2020.100936).

- [20] Higaki H, Takigawa T, Urayama K. 2013. Nonuniform and uniform deformations of stretched nematic elastomers, *Macromolecules* 46, 5223-5231 (doi: 10.1021/ma400771z).
- [21] Kim JH, Lee SE, Kim BH. 2023. Applications of flexible and stretchable three-dimensional structures for soft electronics, *Soft Science* 3, 16 (doi: 10.20517/ss.2023.07).
- [22] Kundler I, Finkelmann H. 1995. Strain-induced director reorientation in nematic liquid single crystal elastomers, *Macromolecular Rapid Communications* 16, 679-686 (doi: 10.1002/marc.1995.030160908).
- [23] Kundler I, Finkelmann H. 1998. Director reorientation via stripe-domains in nematic elastomers: influence of cross-link density, anisotropy of the network and smectic clusters, *Macromolecular Chemistry and Physics* 199(4), 677-686 (doi: 10.1002/(SICI)1521-3935(19980401)199:4<677::AID-MACP677>3.0.CO;2-E).
- [24] Küpfer J, Finkelmann H. 1991. Nematic liquid single crystal elastomers, *Die Makromolekulare Chemie, Rapid Communications* 12, 717-726 (doi: 10.1002/marc.1991.030121211).
- [25] Küpfer J, Finkelmann H. 1994. Liquid crystal elastomers: Influence of the orientational distribution of the crosslinks on the phase behaviour and reorientation processes, *Macromolecular Chemistry and Physics* 195, 1353-1367 (doi: 10.1002/macp.1994.021950419).
- [26] Li M, Yan Y, Xu S, Wang G, Wu J, Feng XQ. 2022. Surface effect on the necking of hyperelastic materials, *Current Applied Physics* 38, 91-98 (doi: 10.1016/j.cap.2022.03.010).
- [27] Luo C, Calderer MC. 2012. Numerical study of liquid crystal elastomers by a mixed finite element method, *European Journal of Applied Mathematics* 23, 121-154 (doi: 10.1017/S0956792511000313).
- [28] Maas SA, Ellis BJ, Ateshian GA, Weiss J. 2012. FEBio: Finite Elements for Biomechanics, *Journal of Biomechanical Engineering* 134(1), 011005 (doi: 10.1115/1.4005694).
- [29] Mbanda BL, Ye F, Selinger JV, Selinger RL. 2010. Modeling elastic instabilities in nematic elastomers, *Physical Review E* 82(5), 051701 (doi: 10.1103/PhysRevE.82.051701).
- [30] Mihai LA. 2022. *Stochastic Elasticity: A Nondeterministic Approach to the Nonlinear Field Theory*, Springer Cham, Switzerland (doi: <https://doi.org/10.1007/978-3-031-06692-4>).
- [31] Mihai LA. 2023. A theoretical model for power generation via liquid crystal elastomers, *Mathematics and Mechanics of Solids* 29(6), 1198-1215 (doi: 10.1177/10812865231193735).
- [32] Mihai LA, Goriely A. 2020. Likely striping in stochastic nematic elastomers, *Mathematics and Mechanics of Solids* 25(10), 1851-1872 (doi: 10.1177/1081286520914958).
- [33] Mihai LA, Goriely A. 2021. Instabilities in liquid crystal elastomers, *Material Research Society (MRS) Bulletin* 46 (doi: 10.1557/s43577-021-00115-2).
- [34] Mihai LA, Goriely A. 2023. Controllable deformations of unconstrained ideal nematic elastomers, *Journal of Elasticity* (doi: 10.1007/s10659-023-10038-5).
- [35] Mihai LA, Raistrick T, Gleeson HF, Mistry D, Goriely A. 2023. A predictive theoretical model for stretch-induced instabilities in liquid crystal elastomers, *Liquid Crystals* (doi: 10.1080/02678292.2022.2161655).
- [36] Mitchell GR, Davis F, Guo W. 1993. Strain-induced transitions in liquid-crystal elastomers, *Physical Review Letters* 71, 2947-2950 (doi: 10.1103/PhysRevLett.71.2947).
- [37] Mooney M. 1940. A theory of large elastic deformation, *Journal of Applied Physics* 11, 582-592 (doi: 10.1063/1.1712836).

- [38] Petelin A, Čopič M. 2009. Observation of a soft mode of elastic instability in liquid crystal elastomers, *Physical Review Letters* 103, 077801 (doi: 10.1103/PhysRevLett.103.077801).
- [39] Petelin A, Čopič M. 2010. Strain dependence of the nematic fluctuation relaxation in liquid-crystal elastomers, *Physical Review E* 82, 011703 (doi: 10.1103/PhysRevE.82.011703).
- [40] Rivlin RS. 1948. Large elastic deformations of isotropic materials. IV. Further developments of the general theory, *Philosophical Transactions of the Royal Society of London. Series A, Mathematical and Physical Sciences* 241, 379-397 (doi: 10.1098/rsta.1948.0024).
- [41] Rothemund P, Kim Y, Heisser RH, Zhao X, Shepherd RF, Keplinger C. 2021. Shaping the future of robotics through materials innovation, *Nature Materials* 20, 1582-1587 (doi: 10.1038/s41563-021-01158-1).
- [42] Sivaloganathan J, Spector SJ. 2011. On the stability of incompressible elastic cylinders in uniaxial extension, *Journal of Elasticity* 105(1-2), 313-330 (doi: 10.1007/s10659-011-9330-9).
- [43] Soltani M, Raahemifar K, Nokhosteen A, Kashkooli FM, Zoudani EL. 2021. Numerical methods in studies of liquid crystal elastomers, *Polymers* 13,1650 (doi: 10.3390/polym13101650).
- [44] Talroze RV, Zubarev ER, Kuptsov SA, Merekalov AS, Yuranova TI, Plate NA, Finkelmann H. 1999. Liquid crystal acrylate-based networks: polymer backbone-LC order interaction, *Reactive and Functional Polymers* 41, 1-11 (doi: 10.1016/S1381-5148(99)00032-2).
- [45] Treloar LRG. 1944. Stress-strain data for vulcanized rubber under various types of deformation, *Transactions of the Faraday Society* 40, 59-70 (doi: 10.1039/TF9444000059).
- [46] Verwey GC, Warner M, Terentjev EM. 1996. Elastic instability and stripe domains in liquid crystalline elastomers, *Journal de Physique II France* 6(9), 1273-1290 (doi: 10.1051/jp2:1996130).
- [47] Warner M, Terentjev EM. 2007. *Liquid Crystal Elastomers*, paper back, Oxford University Press, Oxford, UK.
- [48] White TJ, Broer DJ. 2015. Programmable and adaptive mechanics with liquid crystal polymer networks and elastomers, *Nature Materials* 14, 1087-1098 (doi: 10.1038/nmat4433).
- [49] Zhang Y, Xuan C, Jiang Y, Huo Y. 2019. Continuum mechanical modeling of liquid crystal elastomers as dissipative ordered solids, *Journal of the Mechanics and Physics of Solids* 126, 285-303 (doi: 10.1016/j.jmps.2019.02.018).
- [50] Zubarev ER, Kuptsov SA, Yuranova TI, Talroze RV, Finkelmann H. 1999. Monodomain liquid crystalline networks: reorientation mechanism from uniform to stripe domains, *Liquid Crystals* 26, 1531-1540 (doi: 10.1080/026782999203869).